Article ID: 1006-8775(2026)02-0132-12

Validation and Application Potential of the Sea Surface Temperature Fusion Data from Reprocessed Fengyun-3 Infrared and Microwave Products

ZHANG Miao (张 淼)[1,3,4], LIU Yun-yun (刘芸芸)[2,5], CHEN Lin (陈 林)[1,3,4], XU Na (徐 娜)[1,3,4], CAO Guang-zhen (曹广真)[1,3,4]

(1. National Satellite Meteorological Center (National Centre for Space Weather), China Meteorological Administration, Beijing 100081 China; 2. State Key Laboratory of Climate System Prediction and Risk Management/China Meteorological Administration Climate Studies Key Laboratory, National Climate Centre, China Meteorological Administration, Beijing 100081 China; 3. Innovation Center for FengYun Meteorological Satellite (FYSIC), China Meteorological Administration, Beijing 100081 China; 4. Key Laboratory of Radiometric Calibration and Validation for Environmental Satellite, China Meteorological Administration, Beijing 100081 China; 5. Collaborative Innovation Center on Forecast and Evaluation of Meteorological Disasters, Nanjing University of Information Science & Technology, Nanjing 210044 China)

Abstract: Global sea surface temperature (SST) is a crucial climate element owing to its significant heat capacity and extensive global ocean coverage. This study evaluates an SST fusion dataset derived from Fengyun-3 satellite observations (FY-3_fusion_SST; 2011–2019), with emphasis on its accuracy and potential applications in climate monitoring and operational services. Validation against the operational SST and sea ice analysis (OSTIA_SST) dataset revealed that the accuracy of daily FY-3_fusion_SST data was 0.03±0.55 °C, while that of monthly FY-3_fusion_SST data was 0.02±0.20 °C. Spatially, FY-3_fusion_SST corresponded well with OSTIA_SST in mid-latitude regions and the tropical central-eastern Pacific region, whereas significant differences were observed in the tropical regions of the Atlantic and Indian Oceans and the western Pacific warm pool. In addition, FY-3_fusion_SST and OSTIA_SST data varied in different seasons. The Niño 3.4 index calculated using the FY-3_fusion_SST data effectively characterizes the onset, termination, and intensity of El Niño–Southern Oscillation cycles, although it exhibits a systematic warm bias relative to the index calculated from the Optimal Interpolation SST data. In the tropical regions of the Atlantic and Indian Oceans, the SST indices derived from the FY-3_fusion_SST data exhibited large biases that were comparable to the amplitudes of the SST indices for certain months. These larger SST biases may be due to the influence of strong convective clouds and weak precipitation in tropical regions. In addition, these larger biases may be related to the definitions of the SST indices. When the areas defined by the indices are small, the indices are more prone to large deviations, limiting the application of the FY-3_fusion_SST dataset in climate monitoring and prediction operations.

Key words: sea surface temperature fusion data; Fengyun-3 satellites; El Niño–Southern Oscillation; climate monitoring; validation

CLC number: P405 **Document code:** A

Citation: Zhang, M., Y. Y. Liu, L. Chen, N. Xu, and G. Z. Cao, 2026: Validation and Application Potential of the Sea Surface Temperature Fusion Data from Reprocessed Fengyun-3 Infrared and Microwave Products. *J. Trop. Meteor.*, **32**, 132–143, https://doi.org/10.3724/j.1006-8775.2026.009.

1 INTRODUCTION

The global sea surface temperature (SST) is a critical climate variable owing to its substantial heat capacity and extensive global ocean coverage (Qian et al. 2023). SST anomalies (SSTAs) can induce climate variability by influencing the circulation throughout the troposphere (Pisano et al. 2020). SST has been extensively used in climate monitoring, assessment, prediction, and simulation and plays a key role in applications related to environmental protection, tourism, marine fisheries, and other fields (IPCC 2018; Maguire et al. 2016). As the strongest tropical SST external forcing on seasonal to interannual timescales, the El Niño–Southern Oscillation (ENSO) in the equatorial central-eastern Pacific can trigger severe natural disasters, such as floods, droughts, heat waves, and landslides, which significantly affect lives, property, economic activities, and the natural environment (National Research Council 2010). For instance, ENSO dramatically impacts climate anomalies in East Asia during its various phases (Hu et al. 2005; Liu et al. 2013, 2015, 2024; Wang et al. 2000; Wu et al. 2003; Zhang et al. 1999; Zhang and Sumi 2002; Zhou and Wu 2010). In addition to ENSO, SSTAs in other regions, such as the tropical Indian Ocean (Ding et al. 2021; Wu et al. 2000; Wu and Kirtman 2004), the Atlantic Ocean (Han et al. 2011; Li and Bates 2007; Liu et al. 2020), and the western Pacific warm pool (Nitta and Hu 1996; Guo and

Received 2025-03-13; **Revised** 2025-11-17; **Accepted** 2025-12-23

Funding: National Natural Science Foundation of China (U2442216); Civilian Space Programme of China (D040305)

Biography: ZHANG Miao, associate research fellow, primarily undertaking research on satellite oceanography, and retrieval and fusion of sea surface temperature from FengYun satellite remote sensing.

Corresponding author: LIU Yun-yun, e-mail: liuyuny@cma.gov.cn

Ni 1998), substantially influence the atmospheric circulation and precipitation anomalies in Asia (Zhang et al. 2008). Therefore, high-quality SST data are a prerequisite for investigating SST variations and their corresponding global impacts.

Existing SST observational data, primarily from vessel and buoy observations, cannot meet the demand for large-scale real-time monitoring (Zhao et al. 2024). Satellite-based SST products rely primarily on infrared and passive microwave remote sensing, each with its own set of advantages and limitations. Infrared remote sensing provides SST with high spatial resolution; however, this method cannot be used under cloudy conditions, resulting in low SST coverage (Alerskans et al. 2020; Wentz et al. 2000). Passive microwave sensing enables all-weather observations; however, the SST data retrieved by this method have low spatial resolution and are susceptible to interference from rainfall, coastal proximity, and high wind speeds (Gentemann et al. 2004; Li and Jiang 2024). Therefore, it is necessary to combine the SST data retrieved from infrared and microwave remote sensing to generate accurate SST fields with high resolution and extensive coverage (Yang et al. 2021; Zhang et al. 2024a; Zheng et al. 2008).

Many scholars worldwide have long been engaged in multi-satellite SST fusion research. Major international fusion products include the European Space Agency Climate Change Initiative SST (Merchant et al. 2019), the operational SST and sea ice analysis (OSTIA) SST (Good et al. 2020), the National Oceanic and Atmospheric Administration (NOAA) optimal interpolation SST version 2.1 (OISSTv2.1) (Reynolds et al. 2007), and the Canadian Meteorological Center SST (Brasnett and Colan 2016). The primary SST fusion product of China is CODAS-SST, developed by the National Meteorological Information Center based on the China Meteorological Administration (CMA) ocean data analysis system (CODAS). This fusion product primarily relies on SST data from international sources such as the advanced very high resolution radiometer (AVHRR), the visible infrared imaging radiometer suite, and the advanced microwave scanning radiometer (AMSR). Although CODAS-SST incorporates the visible and infrared radiometer (VIRR) SST from China's Fengyun-3 (FY-3) series, the proportion of FY-3 data in the fusion product is small. To enhance the autonomy of the SST products in China, Zhang et al. (2024a) developed a fusion SST product based on the FY-3 series.

The FY-3 series is China's second-generation polar-orbiting meteorological satellite fleet, of which the FY-3A and FY-3B satellites (first batch) are experimental and the FY-3C, FY-3D, FY-3E, and FY-3F satellites (second batch) are operational. FY-3C/F are morning orbits, FY-3D are afternoon orbits, and FY-3E are early morning orbits (Chen et al. 2025). The National Satellite Meteorological Center of the CMA reprocessed and generated the FY-3/VIRR (Liu et al. 2021; Wang et al. 2014; Wang et al. 2020) and microwave radiation imager (MWRI) (Zhang et al. 2018) long-term SST datasets from 2011 to 2019 (Zhang et al. 2024b), and then the fusion SST (FY-3_fusion_SST) dataset based on the VIRR and MWRI datasets was generated using the method of Zhang et al. (2024a). In this study, the accuracy of the FY-3_fusion_SST dataset was assessed, and its potential application in climate monitoring and prediction operations was explored. In addition, the distribution characteristics and potential reasons for the FY-3_fusion_SST data biases were analyzed to provide technical support for its operational application and to offer a reference for further improvement of this dataset.

The remainder of this paper is organized as follows: Section 2 describes the data and validation indicators used in the study; Section 3 provides the temporal and spatial validations and operational applications of the FY-3_fusion_SST dataset; Section 4 analyzes the potential reasons for biases in the SST indices; finally, Section 5 presents the primary findings and conclusions.

2 MATERIALS AND METHODS

2.1 *Data*

2.1.1 FY-3 FUSION DATASET

In this study, the validated dataset was the FY-3_fusion_SST dataset of the FY-3 VIRR and MWRI SST from 2011 to 2019. The temporal coverage of the FY-3 VIRR and MWRI SST is summarized in Table 1. For SST fusion, we combined observations from the FY-3B, FY-3C, and FY-3D satellites and integrated all available SST data for a specified day. First, the biases in the MWRI SST were corrected using a segmented regression method. The MWRI SST was bilinearly interpolated to match the VIRR SST grid at a resolution of 0.05°×0.05°. Finally, data within a ±3-day window centered on the analysis date were prioritized based on data accuracy and spatial resolution, and optimal interpolation was used to obtain this fused SST dataset. The detailed fusion method is described by Zhang et al. (2024a). Due to satellite platform failures, evident regional biases occurred in the data for June 2014, June 2015, August 2015, and October 2015. Therefore, data from these months were not included in this study.

Because climate monitoring operations primarily focus on the variation in the monthly average SSTA, the daily FY-3_fusion_SST data were averaged monthly over time and smoothed to a spatial resolution of 0.25°×0.25°, yielding 103 months of data in the series. The monthly average SSTA is the difference between the SST of a certain month and the climatology (monthly average SST

Table 1. FY-3 VIRR and MWRI time coverage information.

Satellite	VIRR	MWRI
FY-3A	2009/01–2014/04	–
FY-3B	2011/01–2019/12	2010/11–2019/08
FY-3C	2014/01–2019/12	2013/10–2019/12
FY-3D	–	2018/01–2020/05

over 2011–2019). A flowchart of the data processing is shown in Fig. 1, and detailed information on this dataset is presented in Table 2.

2.1.2 OSTIA DATA

To validate the accuracy of the FY-3_fusion_SST data, the OSTIA_SST dataset from the United Kingdom Met Office, with a horizontal resolution of 0.05°×0.05°, was used as the reference. The OSTIA_SST data were generated by fusing multisource observations from buoys, AVHRR, AMSR, a tropical rainfall measurement mission microwave imager, an advanced orbital scanning radiometer (AATSR), and spinning enhanced visible and infrared imagers. All satellite SST observations in the OSTIA_SST dataset were bias-corrected using AATSR data and buoy observations, with root mean square errors (RMSEs) less than 0.3 °C (Good et al. 2020). In this study, we validated the accuracy of the FY-3_fusion_SST dataset over the region 60°S–60°N, 0°–360°.

2.1.3 OISST DATA

To assess the feasibility of the FY-3_fusion_SST data in climate monitoring operations, OISSTv2.1 (Huang et al. 2021; Reynolds et al. 2007), which is widely used in the monitoring operations of the National Climate Center of CMA, was selected as comparative data. This dataset was generated by the National Climatic Data Center of NOAA using optimal interpolation techniques for multisource SST data from ships, buoys, and bias-corrected AVHRR observations, with a horizontal resolution of 0.25°×0.25°. The OISSTv2.1 product has been widely used in global and regional real-time SSTA monitoring and related research (Liu et al. 2021).

2.2 *Method*

Table 3 provides definitions of commonly used SST indices in the SST monitoring operations of the National Climate Center of CMA. In this study, we validated the feasibility of using the FY-3_fusion_SST data for climate monitoring operations through SST indices in key areas.

Table 2. Detailed information on the FY-3_fusion_SST dataset derived from VIRR and MWRI.

Item	Detailed information
Time range	2011/01/03–2019/11/30
Spatial range	0°–360°, 90°S–90°N
Temporal resolution	Daily/monthly
Spatial resolution	Daily data: 0.05°×0.05° Monthly data: 0.25°×0.25°
Data format	Hierarchical data format

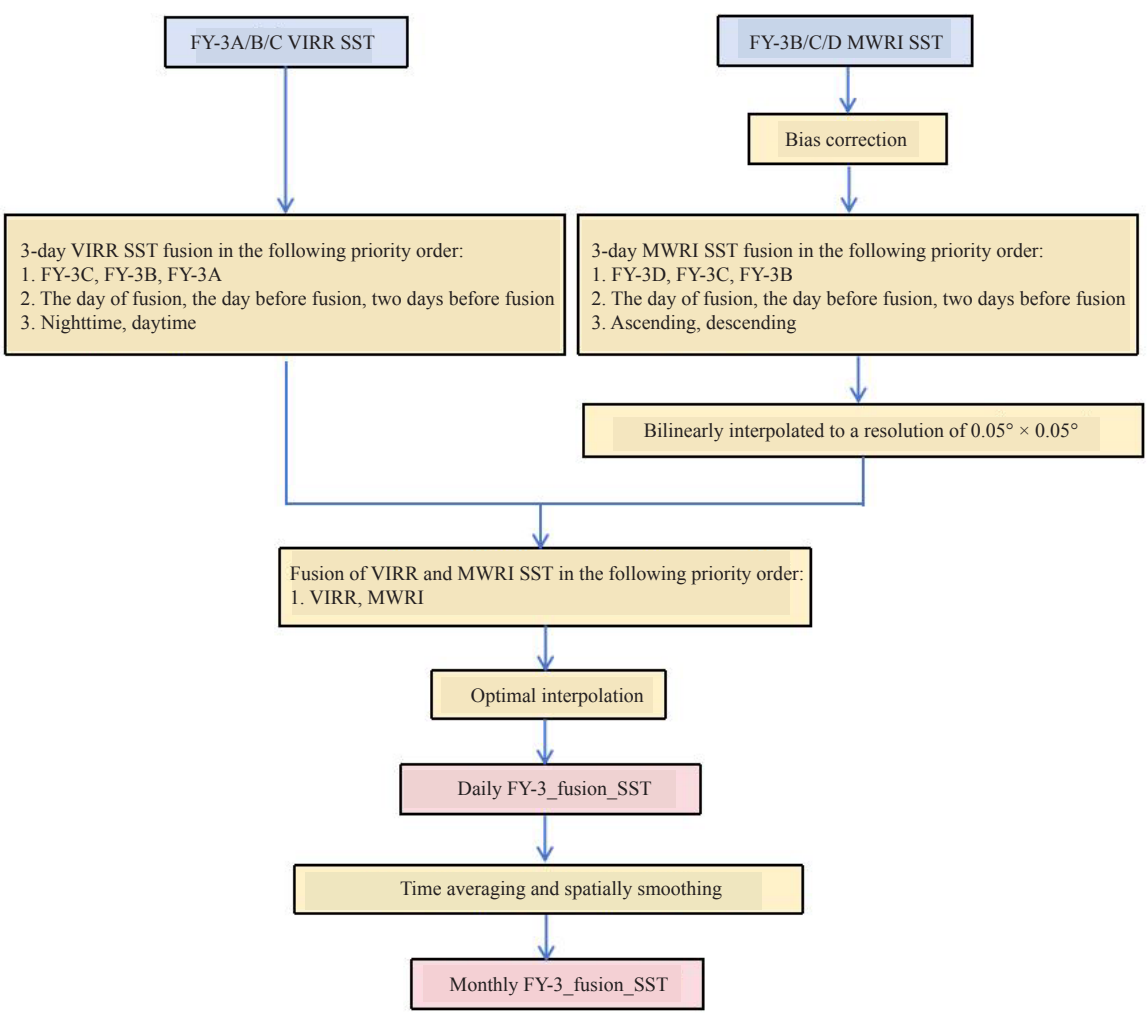


Figure 1. Flowchart of the data processing.

Table 3. Definitions of SST indices in the key areas. "SSTA" denotes SST anomaly.

Index	Definition
Niño 3.4	SSTA in the range of 5°S–5°N, 170°–120°W
Niño 3	SSTA in the range of 5°S–5°N, 150°–90°W
Niño 4	SSTA in the range of 5°S–5°N, 160°E–150°W
Indian Ocean dipole (IOD)	SSTA in the range of 10°S–10°N, 50°–70°E minus SSTA in the range of 10°S–0°, 90°–110°E
Indian Ocean basin mode (IOBM)	SSTA in the range of 20°S–20°N, 40°–110°E
Equatorial Atlantic Niño (ATL3)	SSTA in the range of 3°S–3°N, 20°W–0°
Tropical North Atlantic (TNA)	SSTA in the range of 5°–20°N, 60°–30°W
Tropical South Atlantic (TSA)	SSTA in the range of 20°S–0°, 30°W–10°E
Tropical Atlantic dipole (TAD)	$SSTA_{TNA}-SSTA_{TSA}$

The climatology of the OISSTv2.1 data was calculated as the monthly mean SST during the 2011–2019 period, and the SSTA based on the OISST data was defined as the SST difference between the monthly SST value and the climatology.

The indicators used for accuracy validation and climate application assessment include bias, RMSE, and the correlation coefficient (R). The formulas are as follows:

$$\text{Bias} = \frac{\sum_{i=1}^{m}(X_i - Z_i)}{m} \tag{1}$$

$$\text{RMSE} = \sqrt{\frac{\sum_{i=1}^{m}(X_i - Z_i)^2}{m}} \tag{2}$$

$$R = \frac{\sum_{i=1}^{m}\left(X_i-\overline{X}\right)\left(Y_i-\overline{Z}\right)}{\sqrt{\sum_{i=1}^{m}\left(X_i-\overline{X}\right)^2}\sqrt{\sum_{i=1}^{m}\left(Y_i-\overline{Z}\right)^2}} \tag{3}$$

where i=1, 2, ..., m; m is the total sample size; X is the FY-3_fusion_SST (units: °C); Z is the OSTIA or OISST data (units: °C); $\overline{X}$ is the average of FY-3_fusion_SST (units: °C); and $\overline{Z}$ is the average of the OSTIA or OISST data (units: °C).

3 RESULTS

3.1 *Validation of FY-3_fusion_SST*

The accuracy of the FY-3_fusion_SST data was assessed by analyzing temporal variations and histograms. Overall, FY-3_fusion_SST exhibited warm biases relative to OSTIA_SST, excluding certain short periods during the summer of 2011, the winter of 2014, and the autumn and winter of 2018 (Figs. 2 and 3). On the daily scale, the biases of the FY-3_fusion_SST data varied between −0.08 and 0.20 °C, with an average of 0.03 °C. The RMSEs were in the range of 0.34 °C–0.64 °C, with an average of 0.55 °C (Fig. 4). On the monthly scale, the biases of the FY-3_fusion_SST data were between –0.06 and 0.15 °C, with an average of 0.02 °C. The RMSEs were between 0.16 and 0.26 °C, with an average of 0.20 °C (Fig. 5). The monthly average FY-3_fusion_SST data effectively reduced random errors through spatiotemporal smoothing, making the accuracy superior to that of the daily FY-3_fusion_SST.

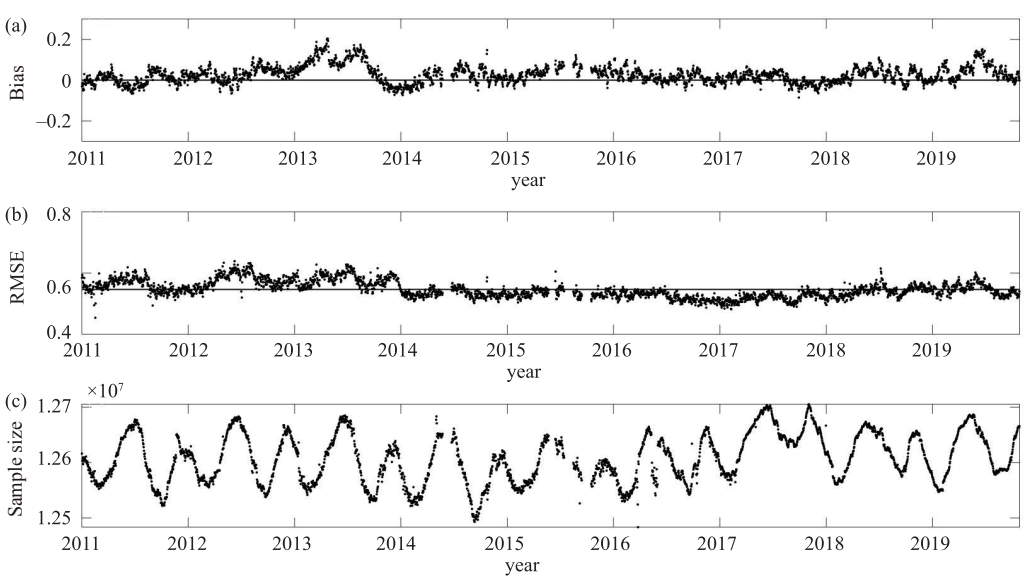


Figure 2. Temporal variations of (a) bias (units: °C), (b) RMSE (units: °C), and (c) sample size of the daily FY-3_fusion_SST (60°S–60°N, 0°–360°) relative to OSTIA_SST data for 2011–2019. The horizontal lines in Figs. 2a and 2b represent the zero-value line and the average-value line, respectively.

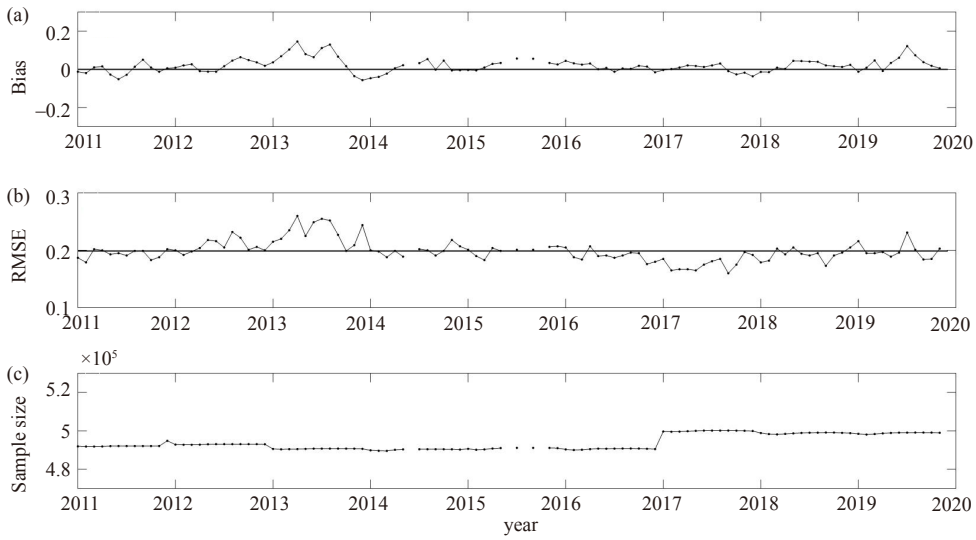


Figure 3. Same as Fig. 2, but for the monthly FY-3_fusion_SST data.

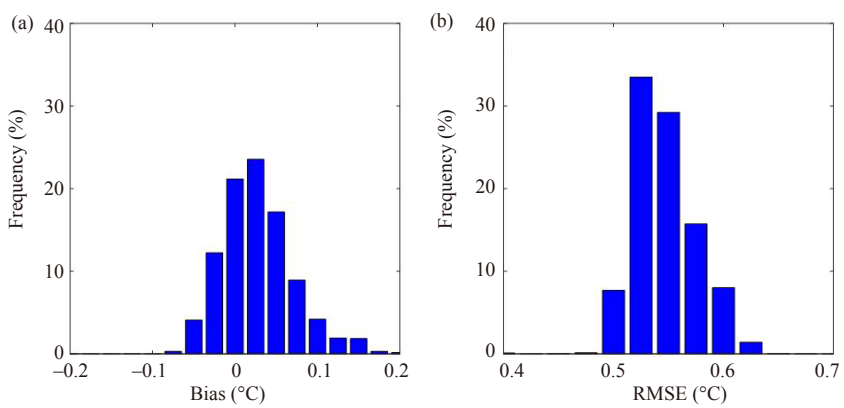


Figure 4. Histograms of (a) bias (units: °C) and (b) RMSE (units: °C) of the daily FY-3_fusion_SST (60°S–60°N, 0°–360°) relative to the OSTIA_SST data for 2011–2019.

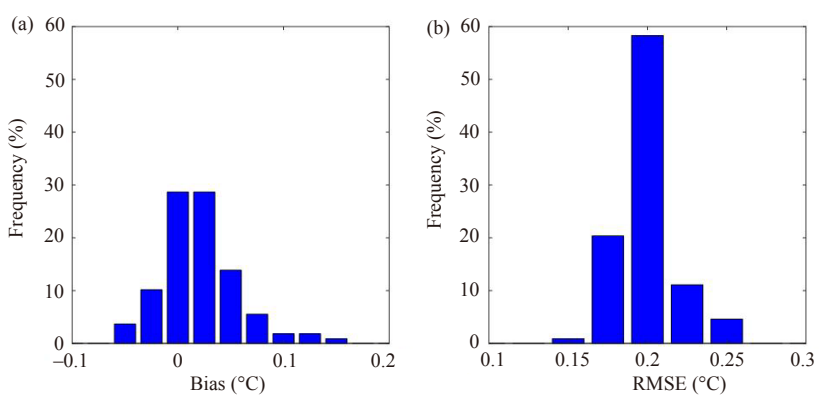


Figure 5. Same as Fig. 4, but for the monthly FY-3_fusion_SST data.

Tables 4 and 5 show that the accuracy of the FY-3_fusion_SST series improved after 2014. The FY-3 VIRR and MWRI SSTs have been validated separately (Wang et al. 2023; Zhang et al. 2024b). The results indicate that the accuracies of FY-3B, FY-3C, and FY-3D MWRI SST are approximately equivalent, and their time series are stable; however, the accuracy of FY-3C VIRR SST is better than that of FY-3B. This improvement is attributed to the inclusion of SST data from the FY-3C VIRR SST since 2014. Before 2014, FY-3_fusion_SST relied solely on FY-3B data. The FY-3B VIRR SST was subject to substantial seasonal fluctuations owing to instrumental performance (Wang et al. 2023), resulting in larger biases.

The spatial characteristics of the biases in the

Table 4. Accuracy verification results for key regions of the daily FY-3_fusion_SST for the periods before and after 2014.

Item	before 2014			after 2014		
	bias (°C)	RMSE (°C)	*R*	bias (°C)	RMSE (°C)	*R*
Tropics (30°S–30°N, 0°–360°)	–0.04	0.51	0.99	0.00	0.50	0.99
Northern Hemisphere midlatitudes (30°N–60°N, 0°–360°)	0.08	0.61	0.99	0.03	0.59	0.99
Southern Hemisphere midlatitudes (60°S–30°S, 0°–360°)	0.06	0.60	0.99	0.05	0.58	0.99
Global (60°S–60°N, 0°–360°)	0.03	0.57	0.99	0.02	0.53	0.99

Table 5. Same as Table 4, but for the monthly FY-3_fusion_SST data.

Item	before 2014			after 2014		
	bias (°C)	RMSE (°C)	*R*	bias (°C)	RMSE (°C)	*R*
Tropics (30°S–30°N, 0°–360°)	–0.02	0.19	0.99	0.01	0.18	0.99
Northern Hemisphere midlatitudes (30°N–60°N, 0°–360°)	0.08	0.23	0.99	0.05	0.22	0.99
Southern Hemisphere midlatitudes (60°S–30°S, 0°–360°)	0.08	0.23	0.99	0.00	0.20	0.99
Global(60°S–60°N, 0°–360°)	0.02	0.21	0.99	0.01	0.20	0.99

monthly FY-3_fusion_SST anomalies relative to OSTIA_SST were further analyzed. Fig. 6 illustrates the distribution of *R*-values in the monthly SSTA between the two datasets. The *R*-value in most areas exceeded 0.9, particularly reaching 0.95 and above in the tropical regions of the central-eastern Pacific, the eastern and western coasts of the North Pacific, the North Atlantic, and the South Indian Ocean. However, the *R*-values were lower than 0.8 and even below 0.6 in the tropical western Pacific warm pool, the tropical Indian Ocean, the equatorial Atlantic, the southeastern Atlantic coasts, and parts of the northern edge of the Antarctic continent. This result indicates that the FY-3_fusion_SST data align well with OSTIA_SST in mid-latitude regions and the tropical central-eastern Pacific, while there are marked differences between them in the tropical Atlantic Ocean, tropical Indian Ocean, and western Pacific warm pool. Similar conclusions were drawn by Liu et al. (2021) in their quality assessment of FY-3/VIRR SST. These differences may be caused by cloud contamination in the Atlantic, Indian Ocean, and western Pacific warm pool, where VIRR SST availability (defined as the ratio of valid SST observation days to the total number of observation days) is approximately 10% (Fig. 7a). This leads to frequent data gaps in VIRR SST observations and introduces certain biases when compared with MWRI SST-derived values. In contrast, MWRI SST data can partially compensate for these gaps in VIRR SST data, as its SST availability in these regions reaches approximately 30% (Fig. 7b). This improvement stems from the ability of microwaves to penetrate clouds. Consequently, the accuracy of the FY-3_fusion_SST product in these regions is higher than that of the FY-3/VIRR SST alone (Liu et al. 2021).

The spatial distribution characteristics of biases between the FY-3_fusion_SST and OSTIA_SST datasets also exhibited distinct seasonal variations. In this study, January, April, July, and October were selected to

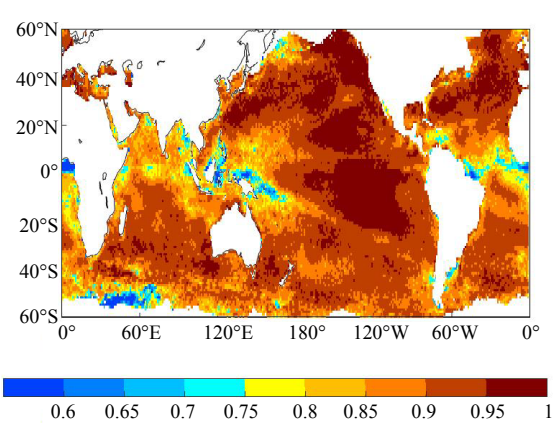


Figure 6. Distribution of *R*-values between the monthly FY-3_fusion_SST anomaly values and the monthly OSTIA_SST anomaly values from January 2011 to November 2019.

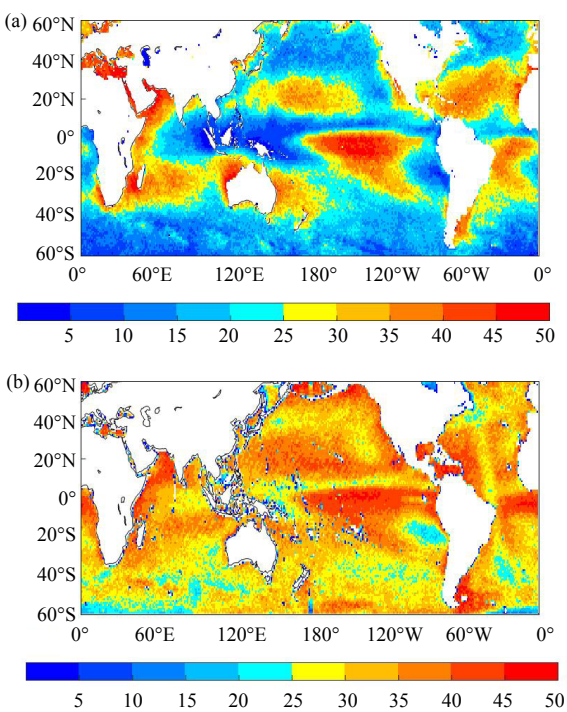


Figure 7. SST availability of (a) FY-3/VIRR and (b) FY-3/MWRI in 2018 (year randomly selected).

represent winter, spring, summer, and autumn, respectively. Fig. 8 shows the spatial distribution of differences between the FY-3_fusion_SST and OSTIA_SST during these seasons. The results indicate that, except for summer, which is predominantly characterized by warm biases, the other three seasons primarily show cold biases, with the most pronounced cold biases occurring in autumn. The average biases for spring, summer, autumn, and winter were 0.01, 0.06, –0.02, and –0.01 °C, respectively. Specifically, in winter, cold biases control regions such as the tropical areas of the Pacific Ocean, the southwestern Pacific, the western Indian Ocean coasts, the tropical Atlantic, and regions north of 40°N and south of 40°S, particularly along the west coast of Africa. In contrast, warm biases are primarily distributed in the tropical East Indian Ocean, the mid-latitude North Pacific, the North Atlantic, the South Indian Ocean, and the Southeast Pacific regions. In spring, the areas with warm biases expand and are more concentrated in the tropical Indian Ocean and the Southern Hemisphere, particularly along the northwestern coast of Australia and the western coast of Mexico. In summer, the range and intensity of warm biases further increased, with considerable positive biases in the Bohai Sea region of China. Cold biases are primarily observed in the tropical Atlantic, the tropical Indian Ocean, the equatorial Southeast Pacific region, and the west coast of Africa. In autumn, areas with cold biases are primarily in the tropical central-eastern Pacific, the tropical Atlantic, the tropical southern Indian Ocean, and regions south of 40°S, while warm biases are concentrated in the mid-latitude North Pacific, the warm pool, the North Atlantic, and the South Pacific. Notably, the Yellow Sea region of China stands out as an anomaly with large biases.

3.2 *Application potential of FY-3_fusion_SST*

As one of the most prominent external forcing signals on an interannual scale, ENSO cycles considerably influence climate anomalies, both in China and globally (Liu et al. 2024; Wang et al. 2000; Wu et al. 2003). In addition, SSTA variations in the tropical Indian Ocean and tropical Atlantic influence atmospheric circulation patterns and climate anomalies in East Asia through thermal and dynamic processes (Ding et al. 2021; Han et al. 2011; Liu et al. 2020; Wu et al. 2000; Wu and Kirtman 2004). Therefore, in climate monitoring and prediction operations, it is crucial to monitor not only the spatial distribution of global SSTAs but also their temporal evolution, which can be represented through the definition of SST indices for key regions (Table 2). In this section, we further compare and analyze several SST indices in key areas based on the FY-3_fusion_SST and OISST data to assess the application potential of the FY-3_fusion_SST data in climate monitoring operations.

According to the definition of El Niño/La Niña events (Ren et al. 2011), an El Niño event is considered if the Niño 3.4 index is ⩾0.5 °C, and this phenomenon lasts for more than 5 months. Conversely, a La Niña event is considered if the Niño 3.4 index is ⩽–0.5 °C, and this phenomenon lasts for more than 5 months. If the peak of the Niño 3 index exceeds that of the Niño 4 index during an ENSO event, it is defined as an Eastern-Pacific-type event, and if the peak of the Niño 4 index exceeds that of the Niño 3 index, it is defined as a Central-Pacific-type event. Fig.5 shows the monthly series of the SST indices (Niño 3.4, Niño 3, and Niño 4) from 2011 to 2019 based

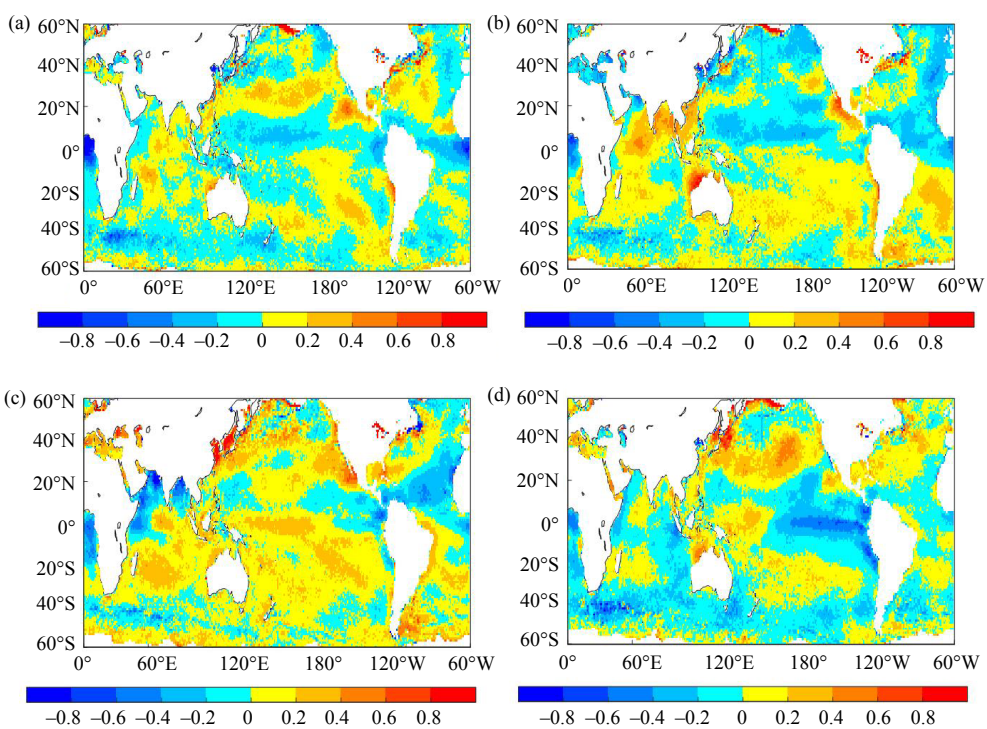


Figure 8. Distributions of the average differences (units: °C) between the FY-3_fusion_SST and OSTIA_SST in (a) January, (b) April, (c) July, and (d) October during 2011–2019.

on the two SST datasets, as well as their biases. The results indicate that from 2011 to 2019, two El Niño events (an extremely strong Eastern-Pacific-type El Niño from October 2014 to April 2016 and a weak Central-Pacific-type El Niño from September 2018 to June 2019) and two La Niña events (a weak Central-Pacific-type La Niña event from August 2011 to March 2012 and a weak Eastern-Pacific-type La Niña event from October 2017 to March 2018) formed in the equatorial regions of the Central–Eastern Pacific Ocean. The Niño 3.4 index derived from FY-3_fusion_SST data effectively reflects the onset and end of each El Niño and La Niña event, as well as the intensity of ENSO events. However, it generally shows warm biases relative to the Niño 3.4 index derived from OISST data, particularly during the super El Niño event, with a maximum warm bias of 0.57 °C (Fig. 9a). The Niño 3 index derived from FY-3_fusion_SST data exhibits similar bias characteristics to the Niño 3.4 index from FY-3_fusion_SST; that is, both indices exhibit warm biases relative to those from OISST data. Subsequently, the peak intensity of the super El Niño event during 2014–2016, based on FY-3_fusion_SST data (2.59 °C), is higher than that based on OISST data (2.53 °C), with the peak occurring in October 2015—three months earlier than the peak in the OISST data (December 2015) (Fig. 9b). The Niño 4 index derived from FY-3_fusion_SST data has a smaller amplitude than the Niño 3.4 and Niño 3 indices, and its average bias is also smaller. The maximum warm biases of the Niño 4 index primarily appeared in December 2013 and February 2014, reaching 0.52 and 0.57 °C, respectively. During these periods, the SST in the equatorial regions of the Central–Eastern Pacific was in a neutral and relatively cold ENSO phase.

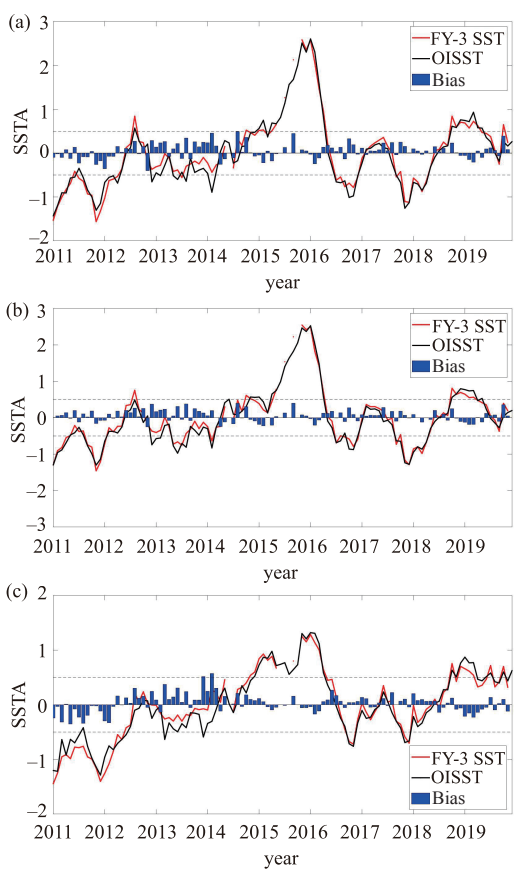


Figure 9. Monthly series (curves; units: °C) of the (a) Niño 3.4, (b) Niño 3, and (c) Niño 4 indices derived from FY-3_fusion_SST and OISSTv2.1 data, with their biases (bars; units: °C) during 2011–2019.

Similarly, Figs. 6 and 7 present comparisons of the historical series of SST indices for the primary circulation modes in the tropical regions of the Atlantic and Indian Oceans, respectively. The IOBM index, one of the key modes in the tropical Indian Ocean, typically lags behind the ENSO cycle by 3–6 months (Chambers et al. 1999; Ding et al. 2021), but its amplitude is smaller than that of the Niño 3.4 index. The results show that the IOBM index derived from the FY-3_fusion_SST data aligns well with that derived from the OISST data and accurately captures the transitions between positive and negative IOBM phases. The cold and warm biases of the IOBM index are both significantly smaller than those of the Niño 3.4 index, with the maximum bias of 0.25 °C appearing in March 2013 (Fig. 10a). However, the biases in the IOD index derived from FY-3_fusion_SST data relative to those derived from OISST data are larger. In certain months, the biases were comparable in magnitude to the IOD index itself, with the maximum value of 0.88 °C appearing in May 2012 (Fig. 10b). From the spatial distribution of global SST biases in different seasons, the tropical Indian Ocean shows both pronounced cold and warm biases (Fig. 8). The IOBM index, which is the average SSTA over the tropical region of the Indian Ocean, offsets the cold and warm biases to a certain extent, resulting in smaller biases. In contrast, the IOD index, which is the difference in SST between the eastern and western parts of the tropical Indian Ocean, exhibits larger biases.

Since the cold biases of FY-3_fusion_SST data in the

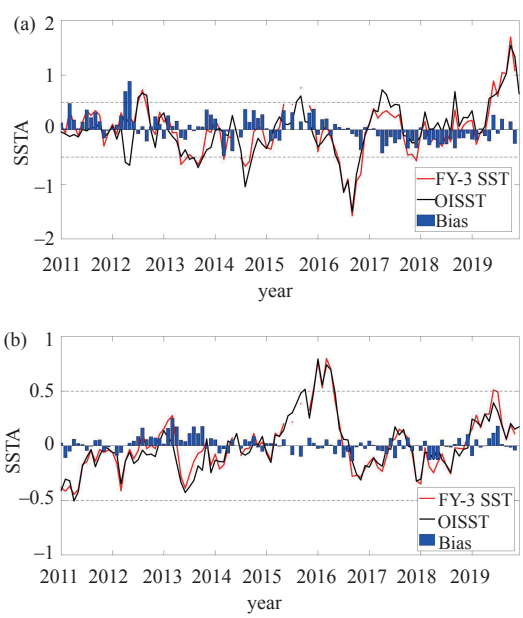


Figure 10. Same as Fig. 9, but for (a) IOD and (b) IOBM.

tropical Atlantic persist across different seasons (Fig. 8), the biases of the four SST indices in the tropical Atlantic are evident (Fig. 11). In addition, these indices show certain advances or lags in the conversion times of the positive and negative phases of the SST modes. The biases of the equatorial Atlantic Niño index even exceeded the index itself in certain months owing to its small defined area (Fig. 11a), with a maximum value of 0.72.

4 DISCUSSION

To explore the potential causes of biases in the SST indices, the El Niño peak period (December 2015) and La Niña trough period (January 2018) were selected for analysis. Fig. 12 shows the spatial distributions of SSTAs based on FY-3_fusion_SST data and their biases relative to those of the OISST data. During the El Niño peak period, the SSTA warm center was in the equatorial parts of the central–eastern Pacific, whereas the warm pool in the western Pacific showed a relatively cold center. Meanwhile, both the tropical Indian Ocean and the tropical Atlantic Ocean exhibited warm anomalies (Fig. 12a). In the tropical part of the central-eastern Pacific, the SST biases north and south of the equator are cold and warm, respectively, with the equator nearly serving as a boundary. Therefore, the average bias of the Niño 3.4 index is relatively small because of the offset between the warm and cold biases. Similarly, in the tropical part of the Indian Ocean, owing to the evident cold biases in the east and warm biases in the west within the basin, the average bias of the IOBM index is relatively small, whereas that of the IOD index is relatively large. In the tropical Atlantic, the biases are distributed as warm to the north of the equator and cold to the south, with the magnitudes of the biases comparable to the SSTA in this region. This led to evident biases in the SST indices related to the Atlantic Ocean (Fig. 12b).

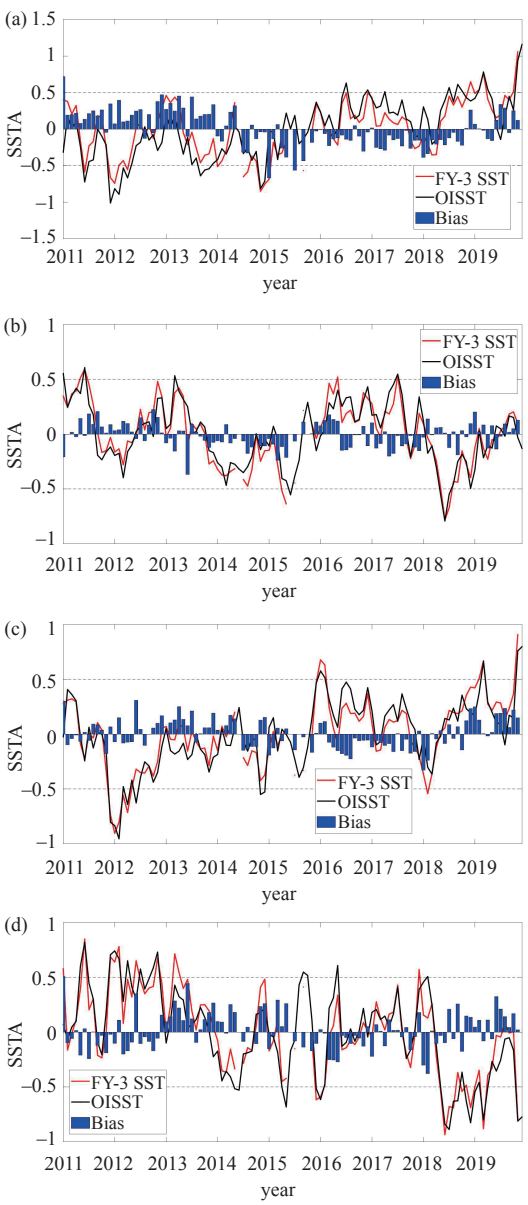


Figure 11. Same as Fig. 9, but for (a) ATL3, (b) TNA, (c) TSA, and (d) TAD.

During the La Niña trough period, the spatial distribution of the SSTA field was nearly the opposite of that during the El Niño peak period; that is, the equatorial parts of the central-eastern Pacific corresponded to the cold center of the SSTA, while the warm pool area corresponded to the warm center. Simultaneously, the tropical regions of the Atlantic and Indian Oceans were controlled by cold anomalies (Fig. 12c). Interestingly, the distribution of SST biases was similar to that during the El Niño peak period, but with weaker biases in the tropical Pacific and tropical Indian Ocean, which may be associated with the weaker intensity of the La Niña event itself. There were evident cold bias centers in the tropical South Atlantic, with biases in some areas exceeding the magnitude of the SSTA itself (Fig. 12d). Overall, the larger SST biases in the tropical regions of the Atlantic and Indian Oceans were likely due to strong convective clouds and weak precipitation in the tropical zone. In addition, larger SST biases may be related to the definitions of the SST indices. When the areas defined by an SST index are extensive, and there is an offset between the cold and warm biases within these regions, the index can capture the temporal variability of the SST in these regions to a certain extent. However, when the defined area of an index is small, biases are more likely to be pronounced, which limits the applicability of FY-3_fusion_SST data in climate monitoring and prediction operations.

5 CONCLUSION

This study focused on a global SST fusion dataset (FY-3_fusion_SST) derived from FY-3/VIRR and MWRI observations. Using OSTIA_SST data from the United Kingdom Met Office and OISST data from the NOAA as benchmarks, we validated the accuracy of the FY-3_fusion_SST dataset and its application potential in climate monitoring and prediction operations. The primary findings of this study are summarized below.

FY-3_fusion_SST and OSTIA_SST data showed

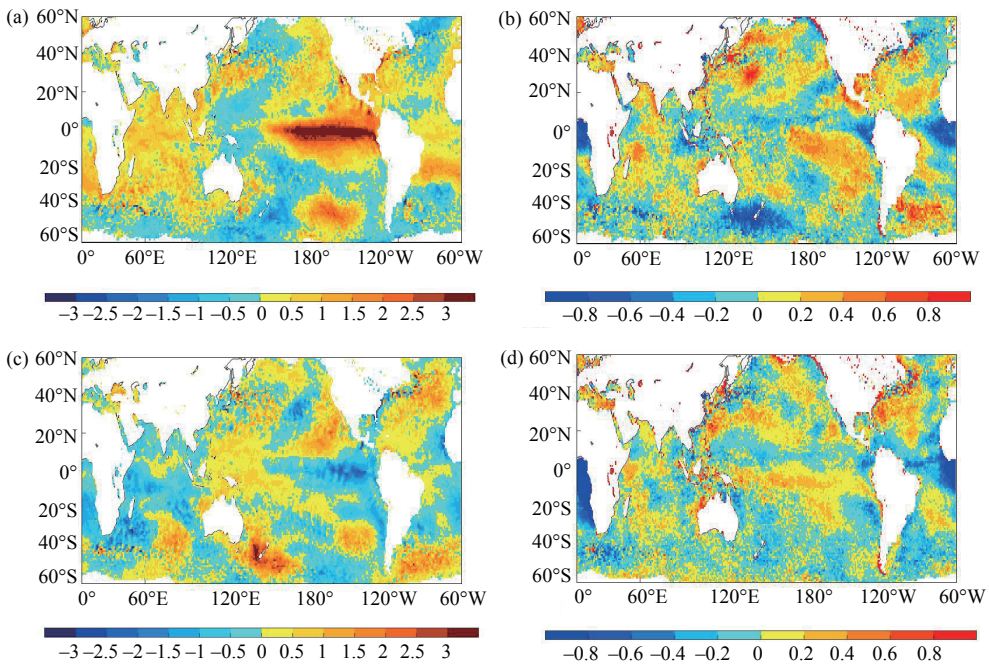


Figure 12. Spatial distributions of (a) FY-3_fusion_SST anomaly values (units: °C) and (b) their biases relative to OISSTv2.1 anomaly data (units: °C) during December 2015, as well as (c, d) the corresponding spatial distributions (units: °C) during January 2018.

good overall consistency from 2011 to 2019; however, regional and seasonal differences were evident. The monthly average FY-3_fusion_SST data, which effectively reduces random errors through spatiotemporal smoothing, generally exhibited higher accuracy than the daily FY-3_fusion_SST data, making them more suitable for supporting climate monitoring and prediction operations. Monthly FY-3_fusion_SST data generally showed warm biases relative to those of OSTIA_SST data, with data stability improving considerably after 2014. FY-3_fusion_SST data aligned well with OSTIA_SST data in mid-latitude regions and the tropical parts of the central-eastern Pacific Ocean, but exhibited evident differences in the warm pool of the western Pacific and the tropical regions of the Atlantic and Indian Oceans. The FY-3_fusion_SST and OSTIA_SST data also varied significantly across seasons.

The Niño 3.4 index derived from FY-3_fusion_SST data can better characterize the onset and end of each El Niño and La Niña event, as well as the intensity of ENSO events, but generally shows warm biases relative to those of the Niño 3.4 index derived from OISST data. In the tropical regions of the Atlantic and Indian Oceans, the SST indices derived from FY-3_fusion_SST data exhibit large biases, which in several months are even comparable to the amplitude of the SST index itself. These larger biases are primarily due to the influence of strong convective clouds and weak precipitation in the tropical zone. In addition, they may also be related to the definitions of the SST indices. That is, when the defined areas of an SST index are large, and there is an offset between the cold and warm biases in these areas, the index can capture the temporal variability of the SST in these regions to a certain extent. When the defined areas of an SST index are small, biases are more likely to be pronounced, which limits the use of FY-3_fusion_SST data in climate monitoring and prediction operations.

The quality assessment of FY-3_fusion_SST data in this study provides a reference for its application in climate monitoring and prediction operations and offers guidance for improving FY-3_fusion_SST data. Compared with using FY-3C/VIRR SST alone, the inclusion of MWRI SST data in the FY-3_fusion_SST dataset effectively reduces the influence of cloud contamination. Currently, this dataset does not account for diurnal variations (Gentemann et al. 2003; Jia et al. 2023). Future adjustments to correct the data to fixed local times unaffected by diurnal variations, such as 10:30 a.m. or 10:30 p.m. (Merchant et al. 2019), could further enhance its applicability in climate studies. However, climatology calculations require temporal averaging over monthly periods. Diurnal cycle errors are categorized as “high-frequency random errors” and are significantly offset at time scales of a monthly average or longer. Thus, they do not affect the conclusion that “the fused dataset is suitable for long-term climatological analysis”. In the future, we will compare this dataset with other SST datasets to further contextualize the performance of the FY-3_fusion_SST dataset.

Acknowledgements: The authors thank NSMC/CMA, E. U. CMEMS, and STAR/NESDIS/NOAA for providing the data used in this research.

Data Availability Statement: All data used in this study are publicly available. The SST fusion of FY-3 is available

at https://satellite.nsmc.org.cn (accessed on December 10, 2024). The OSTIA SST data are available at https://data.marine.copernicus.eu/product/ (accessed on July 1, 2024). The OISST data are available at https://psl.noaa.gov/data/gridded/ (accessed on July 1, 2024).

REFERENCES

Alerskans, E., J. L. Høyer, C. L. Gentemann, L. T. Pedersen, and R. Willatt, 2020: Construction of a climate data record of sea surface temperature from passive microwave measurements. *Remote Sens. Environ.*, **236**, 111485, https://doi.org/10.1016/j.rse.2019.111485.

Brasnett, B., and D. S. Colan, 2016: Assimilating retrievals of sea surface temperature from VIIRS and AMSR2. *J. Atmos. Ocean. Technol.*, **33**, 361–375, https://doi.org/10.1175/jtech-d-15–0093.1.

Chambers, D. P., B. D. Tapley, and R. H. Stewart, 1999: Anomalous warming in the Indian Ocean coincident with El Niño. *J. Geophys. Res.*, **104**, 3035–3047, https://doi.org/10.1029/1998jc900085.

Chen, L., and Coauthors, 2025: FengYun satellites: From observations to quantitative applications. *Natl. Remote Sens. Bull.*, **29**, 1462–1479, https://doi.org/10.11834/jrs.20254459.

Ding, Y. H., Y. Y. Liu, and Z. Z. Hu, 2021: The record-breaking Mei-yu in 2020 and associated atmospheric circulation and tropical SST anomalies. *Adv. Atmos. Sci.*, **38**, 1980–1993, https://doi.org/10.1007/s00376–021–0361–2.

Gentemann, C. L., C. J. Donlon, A. C. Stuart-Menteth, and F. K. Wentz, 2003: Diurnal signals in satellite sea surface temperature measurements. *Geophys. Res. Lett.*, **30**, 1140, https://doi.org/10.1029/2002GL016291.

Gentemann, C. L., F. J. Wentz, C. A. Mears, and D. K. Smith, 2004: In situ validation of Tropical Rainfall Measuring Mission microwave sea surface temperatures. *J. Geophys. Res.*, **109**, C04021, https://doi.org/10.1029/2003jc002092.

Good, S., and Coauthors, 2020: The current configuration of the OSTIA system for operational production of foundation sea surface temperature and ice concentration analyses. *Remote Sens.*, **12**, 720, https://doi.org/10.3390/rs12040720.

Guo, Y., and Y. Ni, 1998: Effects of the tropical Pacific convective activities on China's winter monsoon. *Meteor. Mon.*, **24**, 3–7, https://doi.org/10.7519/j.issn.1000–0526.1998.9.001. (in Chinese)

Han, Z., S. L. Li, and M. Mu, 2011: The role of warm North Atlantic SST in the formation of positive height anomalies over the Ural Mountains during January 2008. *Adv. Atmos. Sci.*, **28**, 246–256, https://doi.org/10.1007/s00376–010–0069–1.

Hu, Z. Z., R. G. Wu, L. J. Kinter III, and S. Yang, 2005: Connection of summer rainfall variations in South and East Asia: Role of El Niño-southern oscillation. *Int. J. Climatol.*, **25**, 1279–1289, https://doi.org/10.1002/joc.1159.

Huang, B. Y., C. Y. Liu, V. Banzon, E. Freeman, G. Graham, B. Hankins, T. Smith, and H. M. Zhang, 2021: Improvements of the daily optimum interpolation sea surface temperature (DOISST) version 2.1. *J. Climate*, **34**, 2923–2939, https://doi.org/10.1175/jcli-d-20–0166.1.

Intergovernmental Panel on Climate Change (IPCC), 2018: Special report: Global warming of 1.5°C. https://www.ipcc.ch/site/assets/uploads/sites/2/2019/06/SR15_Full_Report_Low_Res.pdf.

Jia, C., P. J. Minnett, and B. K. Luo, 2023: Significant diurnal warming events observed by saildrone at high latitudes. *J. Geophys. Res. Ocean.*, **128**, e2022JC019368, https://doi.org/10.1029/2022JC019368.

Li, S., and G. T. Bates, 2007: Influence of the Atlantic multidecadal oscillation on the winter climate of East China. *Adv. Atmos. Sci.*, **24**, 126–135, https://doi.org/10.1007/s00376–007–0126–6.

Li, Z. C., and G. M. Jiang, 2024: Sea surface temperature retrieval from the FY-3D MWRI measurements. *IEEE Trans. Geosci. Remote Sens.*, **62**, 4201010, https://doi.org/10.1109/TGRS.2023.3346819.

Liu, Y. Y., Y. H. Ding, H. Gao, and W. J. Li, 2013: Tropospheric biennial oscillation of the western Pacific subtropical high and its relationships with the tropical SST and atmospheric circulation anomalies. *Chin. Sci. Bull.*, **58**, 3664–3672, https://doi.org/10.1007/s11434–013–5854–7.

Liu, Y. Y., Z. Z. Hu, A. Kumar, P. Peng, D. Collins, and B. Jha, 2015: Tropospheric biennial oscillation of summer monsoon rainfall over East Asia and its association with ENSO. *Climate Dyn.*, **45**, 1747–175, https://doi.org/10.1007/s00382–014–2429–5.

Liu, Y. Y., Z. Z. Hu, and R. G. Wu, 2020: Cooperative effects of tropical Pacific and Atlantic SST forcing in Southern China winter precipitation variability. *Climate Dyn.*, **55**, 2903–2919, https://doi.org/10.1007/s00382–020–05430-z.

Liu, Y. Y., S. J. Wang, J. Liu, Z. S. Gong, and X. L. Jia, 2021: Evaluation of FY-3/VIRR sea surface temperature data for climate applications. *J. Meteor. Res.*, **35**, 952–963, https://doi.org/10.1007/s13351–021–1055–5.

Liu, Y. Y., Z. Z. Hu, R. G. Wu, Y. Ding, and B. Jha, 2024: Evolution of ENSO-related seasonal precipitation anomalies in East Asia: A robustness revisit. *Int. J. Climatol.*, **44**, 269–285, https://doi.org/10.1002/joc.8327.

Maguire, A. J., M. Kolian, K. Rosseel, A. Crimmins, and L. Bacanskas, 2016: Climate change indicators in the United States. United States Environmental Protection Agency.

Merchant, C. J., and Coauthors, 2019: Satellite-based time-series of sea-surface temperature since 1981 for climate applications. *Sci. Data*, **6**, 223, https://doi.org/10.1038/s41597–019–0236-x.

National Research Council, 2010: Assessment of intraseasonal to interannual climate prediction and predictability. National Academies Press.

Nitta, T., and Z. Z. Hu, 1996: Summer climate variability in China and its association with 500 hPa height and tropical convection. *J. Meteor. Soc. Japan*, **7**, 425–445, https://doi.org/10.2151/jmsj1965.74.4_425.

Pisano, A., S. Marullo, V. Artale, F. Falcini, and B. B. Nardelli, 2020: New evidence of Mediterranean climate change and variability from sea surface temperature observations. *Remote Sens.*, **12**, 132, https://doi.org/10.3390/rs12010132.

Qian, Z. L., J. H. Ma, and Z. C. Yin, 2023: Impacts of the SSTs over equatorial central-eastern Pacific and southeastern Indian Ocean on the cold and rainy/snowy/icy weather in Southern China. *J. Meteor. Res.*, **37**, 248–261, https://doi.org/10.1007/s13351–023–2128–4.

Ren, H., and F. F. Jin, 2011: Niño indices for two types of ENSO. *Geophys. Res. Lett.*, **38**, L04704, https://doi.org/10.1029/2010GL046031.

Reynolds, R. W., T. M. Smith, C. Y. Liu, D. B. Chelton, K. S. Casey, and M. G. Schlax, 2007: Daily high-resolution-blended analyses for sea surface temperature. *J. Climate*, **20**, 5473–5496, https://doi.org/10.1175/2007jcli1824.1.

Wang, B., R. G. Wu, and X. H. Fu, 2000: Pacific-East Asian teleconnection: How does ENSO affect East Asian climate? *J. Climate*, **13**, 1517–1536, https://doi.org/10.1175/1520–0442(2000)013<1517:peathd>2.0.co;2.

Wang, S. J., P. Cui, P. Zhang, M. N. Ran, F. Lu, and W. H. Wang, 2014: The improvement of FY-3B/VIRR SST algorithm and its accuracy. *J. Appl. Meteor. Sci.*, **25**, 701–710. (in Chinese)

Wang, S. J., and Coauthors, 2020: FY-3C/VIRR sea surface temperature products and quality validation. *J. Appl. Meteor. Sci.*, **31**, 729–739, https://doi.org/10.11898/1001–7313.20200608.

Wang, S. J., P. Cui, P. Zhang, M. N. Ran, N. Xu, and L. Chen, 2023: The FY-3/VIRR reprocessing sea surface temperature dataset V1.0. Zenodo. Accessed 1 April 2024, https://doi.org/10.5281/zenodo.17173878.

Wentz, F. J., C. Gentemann, D. Smith, and D. Chelton, 2000: Satellite measurements of sea surface temperature through clouds. *Science*, **288**, 847–850, https://doi.org/10.1126/science.288.5467.847.

Wu, G. P., P. Liu, Y. M. Liu, and W. P. Li, 2000: Impacts of the sea surface temperature anomaly in the Indian Ocean on the subtropical anticyclone over the western Pacific two-stage thermal adaptation in the atmosphere. *Acta Meteor. Sinica.*, **58**, 513–522, https://doi.org/10.11676/qxxb2000.054. (in Chinese)

Wu, R. G., Z. Z. Hu, and B. P. Kirtman, 2003: Evolution of ENSO-related precipitation anomalies in East Asia and the processes. *J. Climate*, **16**, 3742–3758.

Wu, R. G., and B. P. Kirtman, 2004: Understanding the impacts of the Indian Ocean on ENSO variability in a coupled GCM. *J. Climate*, **17**, 4019–4031, https://doi.org/10.1175/1520–0442(2004)017<4019:utioti>2.0.co;2.

Xu, B., J. J. Yu, L. Zhang, C. X. Shi, and Z. J. Zhou, 2018: Research progress of global sea surface temperature fusion. *Adv. Meteor. Sci. Technol.*, **8**, 164–170. (in Chinese)

Yang, C. X., and Coauthors, 2021: Sea surface temperature intercomparison in the framework of the Copernicus climate change service (C3S). *J. Climate*, **34**, 5257–5283, https://doi.org/10.1175/jcli-d-20–0793.1.

Zhao, Y. L., P. Liu, and W. Zhou, 2024: Inter-comparison of SST products from iQuam, AMSR2/GCOM-W1, and MWRI/FY-3D. *Remote Sens.*, **16**, 2034, https://doi.org/10.3390/rs16112034.

Zhang, M., S. J. Wang, D. Y. Qin, H. Qiu, and S. H. Tang, 2018: The inversion and quality validation of FY-3C MWRI sea surface temperature. *J. Remote Sens.*, **22**, 713–722, https://doi.org/10.11834/jrs.20187217.

Zhang, M., N. Xu, and L. Chen, 2024a: Fusion SST from infrared and microwave measurement of FY-3D meteorological satellite. *J. Trop. Meteor.*, **30**, 89–96, https://doi.org/10.3724/j.1006–8775.2024.009.

Zhang, M., L. Chen, N. Xu, and G. Z. Cao, 2024b: Influences of earth incidence angle on FY-3/MWRI SST retrieval and evaluation of reprocessed SST. *J. Trop. Meteor.*, **30**, 230–240, https://doi.org/10.3724/j.1006–8775.2024.021.

Zhang, R., and A. Sumi, 2002: Moisture circulation over East Asia during El Niño episode in northern winter, spring and autumn. *J. Meteor. Soc. Japan*, **80**, 213–227, https://doi.org/10.2151/jmsj.80.213.

Zhang, R. H., A. Sumi, and M. Kimoto, 1999: A diagnostic study of the impact of El Niño on the precipitation in China. *Adv. Atmos. Sci.*, **16**, 229–241, https://doi.org/10.1007/BF02973084.

Zhang, Z. Y., D. Y. Gong, D. Guo, X. Z. He, and Y. N. Lei, 2008: Anomalous winter temperature and precipitation events in southern China. *Acta Geograph. Sinica.*, **63**, 899–912, https://doi.org/10.11821/xb200809001.

Zheng, J. W., D. F. Xu, and M. Q. Xu, 2008: A review of merging methods of all covered high resolution SST. *J. Trop. Oceanogr.*, **27**, 77–82, (in Chinese).

Zhou, L. T., and R. G. Wu, 2010: Respective impacts of the East Asian winter monsoon and ENSO on winter rainfall in China. *J. Geophys. Res.*, **115**, D02107, https://doi.org/10.1029/2009jd012502

Citation: Zhang, M., Y. Y. Liu, L. Chen, N. Xu, and G. Z. Cao, 2026: Validation and Application Potential of the Sea Surface Temperature Fusion Data from Reprocessed Fengyun-3 Infrared and Microwave Products. *J. Trop. Meteor.*, **32**, 132–143, https://doi.org/10.3724/j.1006-8775.2026.009.